Deriving Specifications for Coupling through Dual-Wound Generators

L. J. Rashkin[1*], PhD. EE, J. C. Neely[1], PhD. EE, D. G. Wilson[1], PhD. EE, S. F. Glover[1], PhD. EE, N. Doerry[2], PhD., T. J. McCoy[3], PhD.

[1] *Sandia National Laboratories, Albuquerque, NM, USA*
[2] *NAVSEA, PMS 320, Washington, D.C., USA*
[3] *McCoy Consulting, Box Elder, ND, USA*
* Corresponding Author. Email: lrashki@sandia.gov

Synopsis

Many candidate power system architectures are being evaluated for the Navy's next generation all-electric warship. One proposed power system concept involves the use of dual-wound generators to power both the Port and Starboard side buses using different 3-phase sets from the same machine (Doerry, 2015). This offers the benefit of improved efficiency through reduced engine light-loading and improved dispatch flexibility, but the approach couples the two busses through a common generator, making one bus vulnerable to faults and other dynamic events on the other bus. Thus, understanding the dynamics of cross-bus coupling is imperative to the successful implementation of a dual-wound generator system.

In (Rashkin, 2017), a kilowatt-scale system was analysed that considered the use of a dual-wound permanent magnet machine, two passive rectifiers, and two DC buses with resistive loads. For this system, dc voltage variation on one bus was evaluated in the time domain as a function of load changes on the other bus. Therein, substantive cross-bus coupling was demonstrated in simulation and hardware experiments. The voltage disturbances were attributed to electromechanical (i.e. speed disturbances) as well as electromagnetic coupling mechanisms.

In this work, a 25 MVA dual-wound generator was considered, and active rectifier models were implemented in Matlab both using average value modelling and switching (space vector modulation) simulation models. The frequency dynamics of the system between the load on one side and the dc voltage on the other side was studied. The coupling is depicted in the frequency domain as a transfer function with amplitude and phase and is shown to have distinct characteristics (i.e. frequency regimes) associated with physical coupling mechanisms such as electromechanical and electromagnetic coupling as well as response characteristics associated with control action by the active rectifiers. In addition, based on requirements outlined in draft Military Standard 1399-MVDC, an approach to derive specifications will be discussed and presented. This method will aid in quantifying the allowable coupling of energy from one bus to another in various frequency regimes as a function of other power system parameters. Finally, design and control strategies will be discussed to mitigate cross-bus coupling. The findings of this work will inform the design, control, and operation of future naval warship power systems.

Keywords: Gas Turbine Generators; Dual-Wound Generators; Coupling; Specifications; Marine systems

1. Introduction:

The primary purpose of a dual-wound machine is to supply multiple subsystems from a single compact generator (Hodge, 2015). Several different winding strategies and applications can be applied to dual wound machines (Hodge, 2015), (Mese, 2012). This can even include using two sets of windings with different frequencies to supply a high-powered propulsion load as well as a lower powered service load (Hodge, 2015), but should also allow for redundant systems where one generator can be used to supply power for both port and starboard busses (Doerry, 2015). Dual wound machines can also allow for a single machine to operate in both generation and motoring modes at the same time (Mese, 2013). In some instantiations, this can allow for some simplification of power electronics and enables a connected battery to charge or discharge to one set of windings while the other set of windings is always used to provide power to electrical devices on the system (Mese, 2013). Dual wound machines can also provide better power quality by tighter regulation of stator MMF (Mese, 2012). In all the above cases, the machine windings are made to minimize flux linkages between the phases of different winding sets and their construction can be very different from traditional machines.

The primary engineering challenge with dual wound machines addressed in this work is managing the inductive and electromechanical coupling of the two circuits. Specifically, since the phase currents of both circuits contribute to flux linkage and torque, the loading of one circuit may couple to the other through the stator flux (electromagnetic induction) and/or through transient effects on mechanical speed which in turn affect back-emf (electromechanical). While the electromechanical coupling is somewhat intuitive and easily modelled, the inductive coupling is more challenging. In this work, a 2-zone power system with dual-wound machine was modelled and evaluated in simulation for several fault scenarios. In a previous work, a kilowatt-scale system was

 http://doi.org/10.24868/issn.2631-8741.2018.008

analysed that considered the use of a dual-wound permanent magnet machine, two passive rectifiers, and two DC buses with resistive load (Rashkin, 2017). In another work a 20 MW scale system with active rectifiers, two DC buses and constant power loads was also examined (Rashkin, 2018). In both works, coupling between the two buses were observed based on the generator design.

2. The dual-wound gas turbine generator system

In this work, a two-zone power system, wherein both zones are supplied by a single generator, is evaluated; see Figure 1. The system includes a 20 MW rated gas-turbine generator with speed governor, a dual-wound permanent magnet synchronous machine (PMSM) or a dual-wound wound rotor synchronous machine (WRSM), two active rectifiers with LC output filters, switch gear, and variable resistive loads. Only the PMSM was considered during the analysis contained herein.

The dual-wound generator is a six phase synchronous machine where the outputs are grouped into two sets of phases, *abc* and *xyz*. These outputs can then be used to supply two separate loads or buses. The dual wound generator is classified by the pitch angle, β, between the phase sets. Two common dual wound machine layouts are shown in Figure 2. A machine with a pitch angle of 60º is referred to as a symmetrical dual-wound machine (SDW) while a machine with a pitch angle of 30º is referred to as an asymmetrical dual wound machine (ADW).

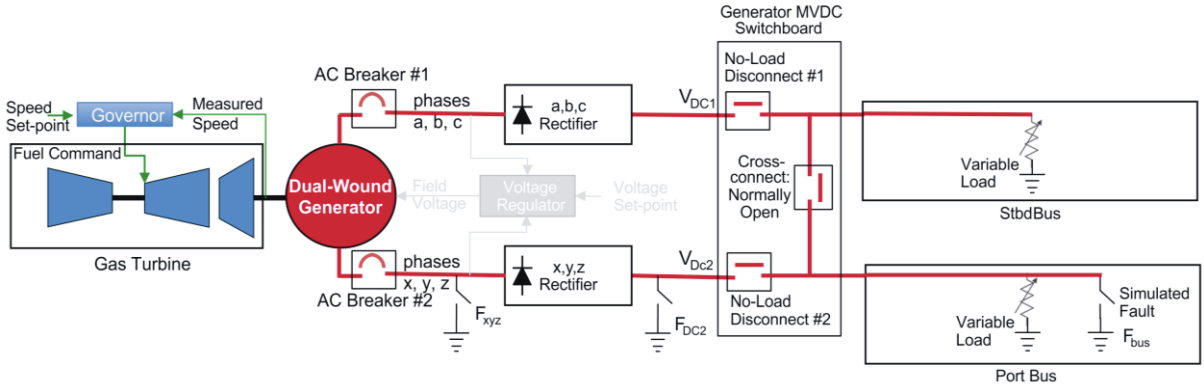

Figure 1: Illustration of Two Power Systems Supplied by a Single Dual Wound Generator

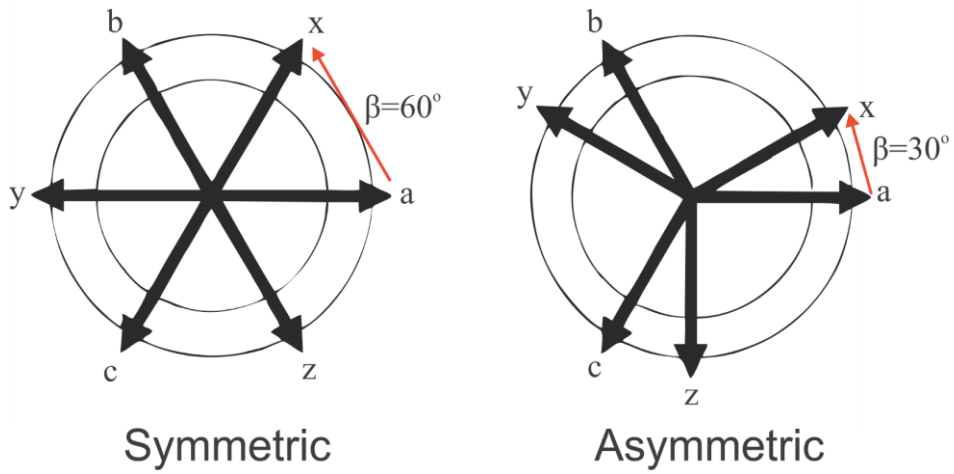

Figure 2: Two Potential Dual-Wound Generator Layouts

2.1. Gas Turbine Model

The gas turbine model is based on a quasi-static empirical model of power flow (Doktorcik, 2011), (Meyer, 2014). The resulting model takes the form:

$$P^*_{fuel} = (c_6 + c_7\omega_{rm} + c_8\omega^2_{rm} + c_9\omega^3_{rm})u_{fuel} + (c_{10} + c_{11}\omega_{rm} + c_{12}\omega^2_{rm} + c_{13}\omega^3_{rm})(1 - u_{fuel}) \quad (1)$$

$$\frac{dP_{fuel}}{dt} = m_{rate}\tanh\left(\frac{P^*_{fuel} - P_{fuel}}{\tau_{fuel} m_{rate}}\right) \quad (2)$$

$$\frac{dP_{comp}}{dt} = k_5 P_{comp} + k_6 P_{fuel} \quad (3)$$

http://doi.org/10.24868/issn.2631-8741.2018.008

$$P_{wf3} = \eta_{comb} P_{fuel} + P_{comp} \tag{4}$$

$$P_{turb} = \left(c_1 + k_1 P_{wf3} + k_2 P_{wf3}^2\right)\omega_{rm} + \left(k_3 P_{wf3} + k_4 P_{wf3}^2\right)\omega_{rm}^2 \tag{5}$$

where P_{fuel}^* and P_{fuel} are the commanded and actual fuel power (rate of chemical energy delivered), P_{comp} and P_{wf3} are the power at the compressor and output shaft, u_{fuel} is the normalized control input between 0 and 1, m_{rate} is the maximum rate of change of fuel power, τ_{fuel} is the time constant of the fuel rate, and η_{comb} is the combustion efficiency.

The parameters k_1 through k_6 are based on a surface mapping of the relationship between steady state output power, steady state fuel power and steady state speed, and τ_{fuel} and the efficiencies of the compressor, combustor, turbine, and extraction. The parameters c_6 through c_{13} determine polynomial fits to the minimum and maximum fuel power as functions of speed (Doktorcik, 2011). The output torque of the turbine, T_{turb}, can be determined by dividing the turbine output power by the shaft speed:

$$T_{turb} = \frac{P_{turb}}{\omega_{rm}} \tag{6}$$

which can then be used to model the mechanical dynamics of the system.

2.2. Dual-Wound Generator Model

The dual wound generator is modelled in the *qd*-axis by using the transformation

$$K_{s_{abc}}^r = \frac{2}{3}\begin{bmatrix} \cos(\theta_r) & \cos\left(\theta_r - \frac{2\pi}{3}\right) & \cos\left(\theta_r + \frac{2\pi}{3}\right) \\ \sin(\theta_r) & \sin\left(\theta_r - \frac{2\pi}{3}\right) & \sin\left(\theta_r + \frac{2\pi}{3}\right) \\ 1/2 & 1/2 & 1/2 \end{bmatrix} \tag{7}$$

$$K_{s_{xyz}}^r = \frac{2}{3}\begin{bmatrix} \cos(\theta_r - \beta) & \cos\left(\theta_r - \beta - \frac{2\pi}{3}\right) & \cos\left(\theta_r - \beta + \frac{2\pi}{3}\right) \\ \sin(\theta_r - \beta) & \sin\left(\theta_r - \beta - \frac{2\pi}{3}\right) & \sin\left(\theta_r - \beta + \frac{2\pi}{3}\right) \\ 1/2 & 1/2 & 1/2 \end{bmatrix} \tag{8}$$

$$K_s^r = \begin{bmatrix} K_{s_{abc}}^r & 0 \\ 0 & K_{s_{xyz}}^r \end{bmatrix} \tag{9}$$

where β denotes the pitch angle between the *abc*- and *xyz*-set of windings. The machine equations in this reference frame can be written as:

$$v_{qs_{abc}}^r = r_s i_{qs_{abc}}^r + \omega_r \lambda_{ds_{abc}}^r + p\lambda_{qs_{abc}}^r \tag{10}$$

$$v_{qs_{xyz}}^r = r_s i_{qs_{xyz}}^r + \omega_r \lambda_{ds_{xyz}}^r + p\lambda_{qs_{xyz}}^r \tag{11}$$

$$v_{ds_{abc}}^r = r_s i_{ds_{abc}}^r - \omega_r \lambda_{qs_{abc}}^r + p\lambda_{ds_{abc}}^r \tag{12}$$

$$v_{ds_{xyz}}^r = r_s i_{ds_{xyz}}^r - \omega_r \lambda_{qs_{xyz}}^r + p\lambda_{ds_{xyz}}^r \tag{13}$$

$$v_{0s_{abc}}^s = r_s i_{0s_{abc}}^r + p\lambda_{0s_{abc}}^r \tag{14}$$

$$v_{0s_{xyz}}^s = r_s i_{0s_{xyz}}^r + p\lambda_{0s_{xyz}}^r \tag{15}$$

$$\lambda_{qs_{abc}}^r = \left(L_{ls} + \frac{3}{2}L_{ms}\right) i_{qs_{abc}}^r + \frac{3}{2}L_{ms} i_{qs_{xyz}}^r \tag{16}$$

$$\lambda_{qs_{xyz}}^r = \left(L_{ls} + \frac{3}{2}L_{ms}\right) i_{qs_{xyz}}^r + \frac{3}{2}L_{ms} i_{qs_{abc}}^r \tag{17}$$

$$\lambda_{ds_{abc}}^r = \left(L_{ls} + \frac{3}{2}L_{ms}\right) i_{ds_{abc}}^r + \frac{3}{2}L_{ms} i_{ds_{xyz}}^r + \lambda_m' \tag{18}$$

$$\lambda_{ds_{xyz}}^r = \left(L_{ls} + \frac{3}{2}L_{ms}\right) i_{ds_{xyz}}^r + \frac{3}{2}L_{ms} i_{ds_{abc}}^r + \lambda_m' \tag{19}$$

$$\lambda_{0s_{abc}}^r = L_{ls} i_{0s_{abc}}^r \tag{20}$$

$$\lambda_{0s_{xyz}}^r = L_{ls} i_{0s_{xyz}}^r \tag{21}$$

where $f_{qs_{abc}}$, $f_{ds_{abc}}$, and $f_{0s_{abc}}$ denote the variable f from the *abc* set of phases in the *qd0*-axis and $f_{qs_{xyz}}$, $f_{ds_{xyz}}$, and $f_{0s_{xyz}}$ denote the variable f from the *xyz* set of phases in the *qd0*-axis where f can be any three phase variable such as v, i, or λ (Krause, 2002). It is noted that with this transformation, the pitch angle, β, does not have an effect on the *qd*-axis behaviour of the system. The electromagnetic torque may be expressed in the *qd*-axis as (Krause, 2002), (Aghaebramhimi, 1997):

$$T_{elec} = \frac{3}{2}\frac{P}{2}\lambda_m' \left(i_{qs_{abc}}^r + i_{qs_{xyz}}^r\right) \tag{22}$$

wherein *P* is the number of poles, $i_{qs_{abc}}^r$ is the *q*-axis current associated with the *abc* set of phases, $i_{qs_{xyz}}^r$ is the *q*-axis current associated with the *xyz* set of phases, and λ_m' is the flux linkage contributed by the permanent magnet.

http://doi.org/10.24868/issn.2631-8741.2018.008

2.3. Active Rectifier Models

The active rectifiers are based on space-vector modulation (Krause, 2002). In this modulation scheme, first the commanded *qd*-axis voltages are determined by a closed loop control. The system is then transformed into the stationary reference frame and the *q*- and *d*-axis modulation indices, m_q^{s*} and m_d^{s*}, are calculated, creating a modulation vector in the space vector state diagram, see Figure 3. Switching is determined by the sector that the modulation vector falls into and the state vectors that bound that sector. This modulation scheme has the advantage of being devoid of low frequency harmonic content and having a coordination between the switching in all phases.

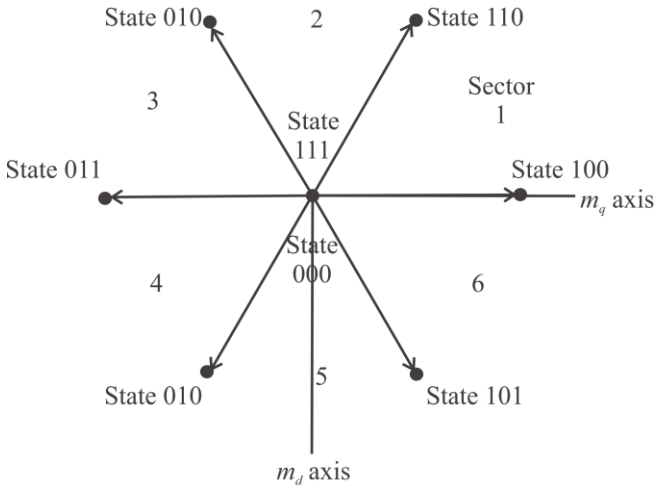

Figure 3: Space Vector State Diagram (Krause, 2002)

3. System Performance Constraints

The power system must operate within a set of designated performance specifications. These specifications typically include several requirements regarding electrical grounding methods, safety, electromagnetic interference / compatibility (EMI and EMC), power quality, efficiency calculation, and transient recovery, among others. In particular, the IEEE Standard 1709 defines an MVDC voltage tolerance worst case envelope for response to faults and also requires the DC voltage to remain within +/-10% of nominal in steady state (IEEE, 2010). Steady state is intended to include normal operating conditions, which in this case, would include the use of pulsed loads.

For a dual wound generator (DWG) based system, the transient response is complicated by the electromagnetic and electromechanical coupling of the two buses through a common generator. One motivation for a multi-bus implementation is to prevent a fault or malfunction on one bus from adversely affecting the entire power system. Thus, for a DWG based system, the isolation between buses should be sufficient such that a fault on one bus does not result in a voltage deviation on the other bus greater than 10% from nominal. To establish that a system has sufficient isolation, a testing protocol is needed to evaluate the system response. Unfortunately, repeated fault tests are likely infeasible, the selection of test parameters is not immediately intuitive, and it is further complicated by the many permutations of possible initial conditions that could affect the system fault response. In fact, there would be great benefit in the implementation of a method that combines a benign test procedure with analysis that allows the fault response to be inferred.

Herein, the time domain transient response is considered, focusing on the criteria defined in IEEE Standard 1709, and the system modelled in Section II. The frequency domain characteristics are determined through measurement (in simulation), and the bounds on the potential time domain response are inferred. In particular, the approach allows for complex scenarios that involve fault events and pulsed load deployment.

http://doi.org/10.24868/issn.2631-8741.2018.008

4. Computing Limits on Coupling and Stimulus

In (Rashkin, 2017), simulation studies were done to characterize the interaction between buses in the frequency domain, with the primary focus being on voltage and current disturbances in response to load power changes. This is often done using sine-sweep (or Chirp) signals and is represented using transfer function matrices, as shown in (39)

$$\begin{bmatrix} Y_1 \\ Y_2 \end{bmatrix} = \begin{bmatrix} H_{11} & H_{12} \\ H_{21} & H_{22} \end{bmatrix} \begin{bmatrix} U_1 \\ U_2 \end{bmatrix} \tag{39}$$

wherein H_{ij} defines the linear system transfer function matrix relating input vector U_j to output vector Y_i. H_{ij} can be found or approximated by sweeping $u_j(t)$ through the frequency range of interest and observing the response in $y_i(t)$, called "sine sweep" or "Chirping". Y_i can be a vector of several quantities. Since the derivation is empirical rather than analytic, it does not matter that different quantities (ie AC, DC, or even speed, …) are included in one vector. The quantities of interest included the following

$$Y_i = \begin{bmatrix} V_{qs,i} & V_{ds,i} & I_{qs,i} & I_{ds,i} & V_{DC,i} \end{bmatrix}^T \tag{40}$$

which includes qd-axis voltages and currents as well as the dc voltage.

(Rashkin, 2018) showed that the construction of the motor could greatly affect the nature of this coupling. Therein, a chirp signal with a frequency range of 0.1 Hz to 10 kHz, and an amplitude of 1 MW, was applied to the load power on the starboard bus, see Figure 4. As shown in Figure 5 and Figure 6 when using a permanent magnet synchronous machine (PMSM) as a generator, there is a significant coupling of the low frequency disturbances on one bus to the other bus through the machine. The higher frequency content of the voltage response is seen in Figure 5 to primarily effect the voltage on the starboard bus, where the chirp is applied. Lower frequency content (i.e. Below 30 Hz) passes through the machine and affects the Port side, but higher frequency content is greatly attenuated. Figure 6 shows this low-pass characteristic in the frequency domain. Because of the potential impact of generator design on the system behaviour, it is therefore useful to derive some design specifications based on the potential coupling of the system.

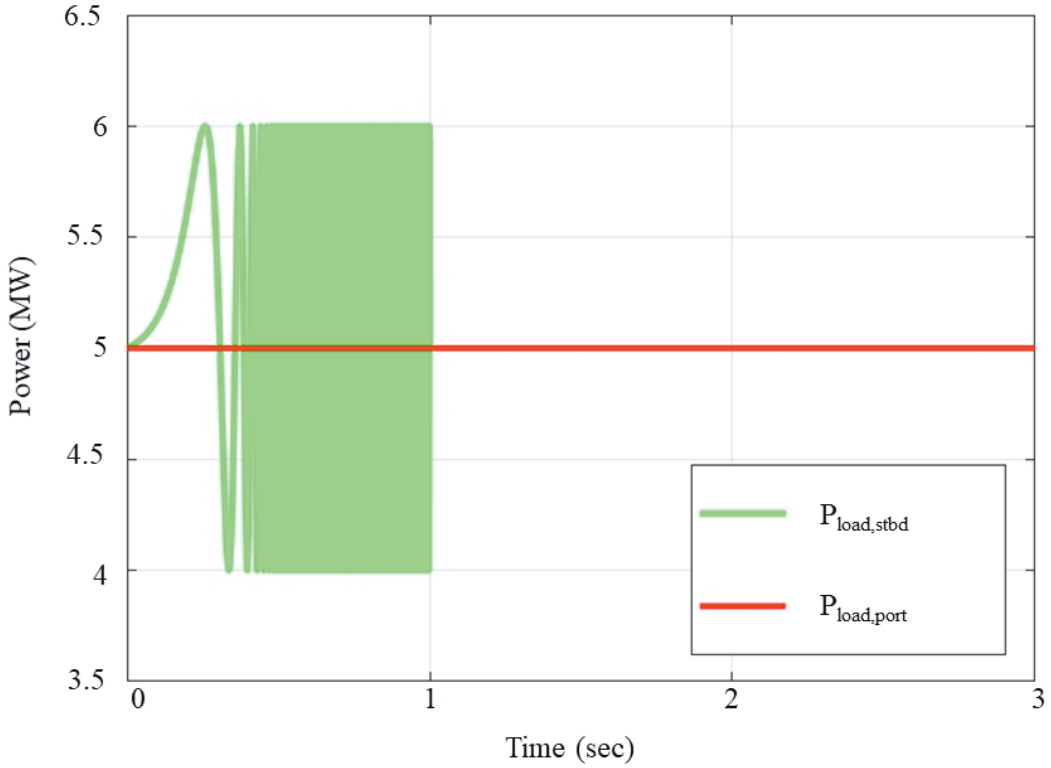

Figure 4: Load power applied to each bus during chirp test

http://doi.org/10.24868/issn.2631-8741.2018.008

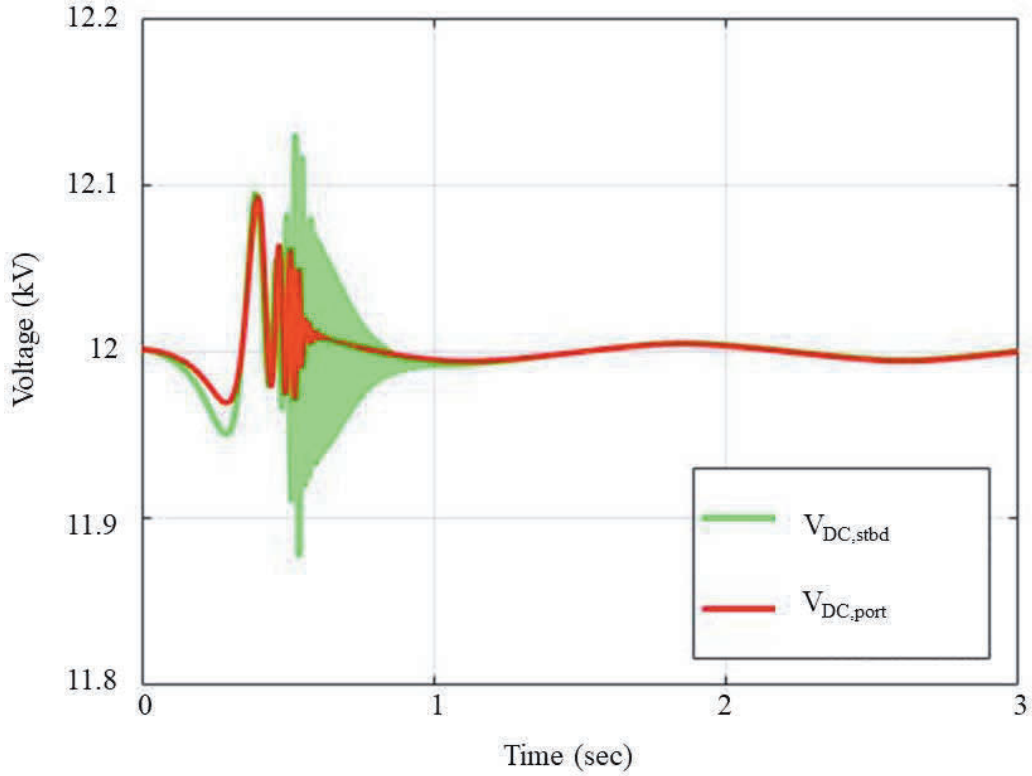

Figure 5: DC Bus Voltage Response with Permanent Magnet Synchronous Machine

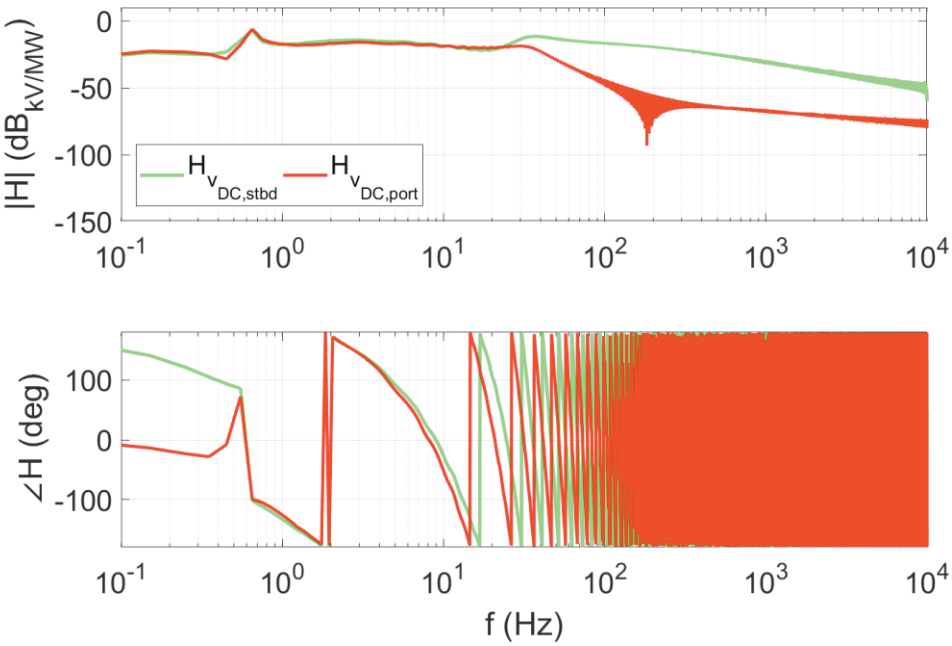

Figure 6: Transfer Function between Stbd. Load and Bus Voltage for Permanent Magnet Synchronous Machine

From this plot the voltage response through the machine can be estimated for a load at a given frequency. Using the constraints on the line voltages, additional constraints on the load stimulus on each bus can then be derived at each frequency. Figure 7 shows the load limits at all frequencies. It should be noted that this limit does not take into account the full spectrum of the load response. It can be seen that for most frequencies, an amplitude equal to the full load of close to 10 MW would be permissible, but there are points where it drops to a 2 MW amplitude. Additionally, at frequencies of over 100 Hz large load magnitudes are allowed due to the larger decoupling between the two buses at higher frequencies. This information can be used to help inform modifications to the

http://doi.org/10.24868/issn.2631-8741.2018.008

specifications found for a single wound machine connected to a single bus. In particular, we wish to characterize the response to fast load transitions (ie. Stepped load) and to faults on the adjacent bus. A favoured approach is to consider a dynamic model of the coupling through the machine.

An approximation to the transfer function $H_{V_{DC,port}}$ was formulated empirically to be

$$H_{vDC,port} \approx \frac{-2.911s^5-3809s^4+42120s^3-1.466e5s^2+1.64e5s}{s^6+115.7s^5+3.173e4s^4+2.175e5s^3+9.079e5s^2+2.373e6s+6.624e5} \quad (41)$$

Figure 8 shows the step response of this transfer function to a unit step (i.e. a 1 MW step in load on the Starboard side); the response indicates a -140 V deviation which swings to a +125 V deviation in Portside dc voltage. By scaling this response, we can estimate the behaviour of the system to a stepped load or to a fault and determine the faulting condition limits based on the coupling through the machine.

To maintain compliance with IEEE Std 1709, the Portside voltage (unfaulted side) should stay within 1200V (10% of nominal); assuming the model scales, this implies a requirement that Starboard side load stepping be limited to approximately 8.5 MW. Similarly, the transfer function in (41) is used to estimate the impulse response. Figure 8 illustrates the Portside voltage deviation in response to a 1 MJ impulse (i.e. a dirac delta, in units of energy). This shows a deviation that swings to -13.5 kV and then to +7.5 kV in response. Assuming the model scales, one can estimate that faulting conditions be limited to 89 kJ to maintain voltage compliance on the unfaulted bus. In the following section, the fault response is investigated through simulation.

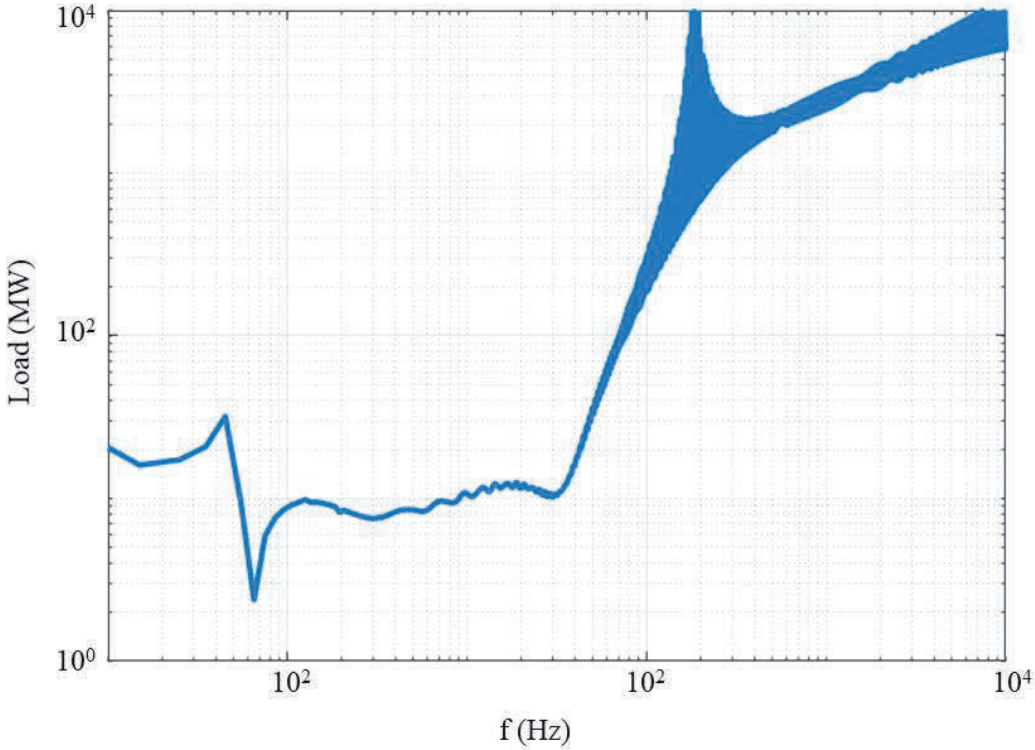

Figure 7: Load Limits as a Function of Frequency

http://doi.org/10.24868/issn.2631-8741.2018.008

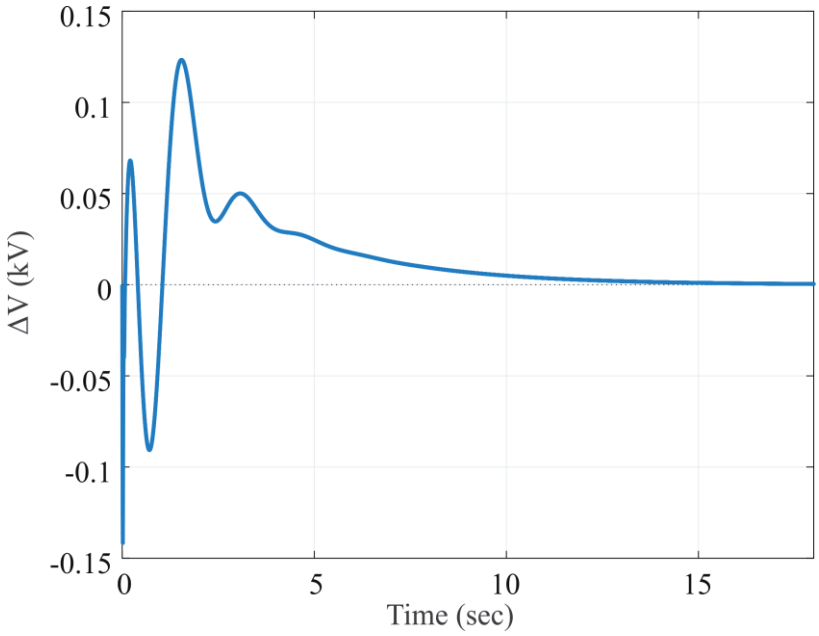

Figure 8: Step Response of Port side dc voltage variation to Starboard side 1 MW load power step; based on empirical transfer function (41)

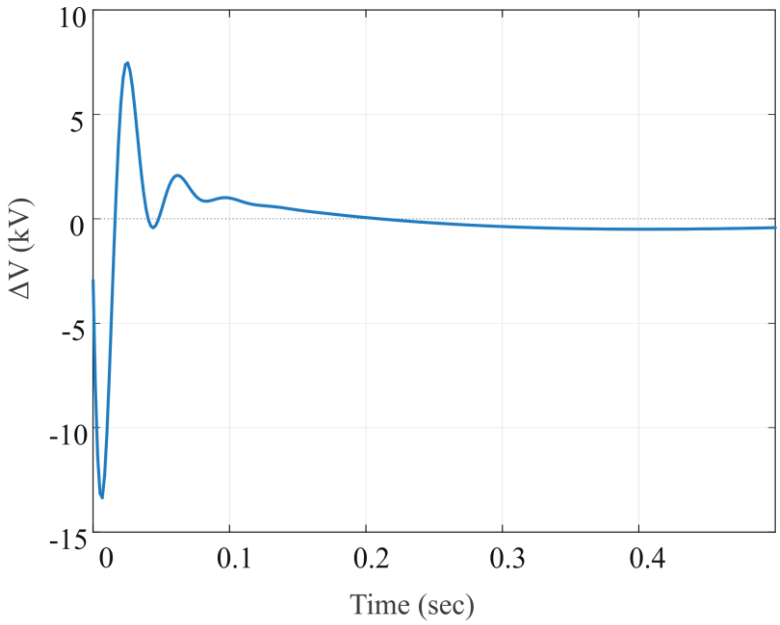

Figure 9: Impulse response of Port side dc voltage variation to Starboard side 1 MJ load impulse; based on empirical transfer function (41)

5. Simulation Example

The system described in Section II was modelled dynamically and simulation models were implemented in Matlab to predict the system response to faults. Specifically, a fault was applied to the starboard DC bus at 5 seconds; this was a 1 Ω fault with a 10 ms duration. Figure 10 shows the simulated bus voltages for the Starboard and Port side buses. Figure 11 shows the equivalent load power for the fault simulation; the energy attributed to the 10 msec fault is 379 kJ. This results in a peak voltage on the Portside of 13.60 kV (deviation is approx. 13.4% of nominal). The simulation is repeated with a 2 Ω fault for 10 msec. The result is a 328 kJ fault energy and a 12.78 kV peak voltage (approx. 8% above nominal). Finally, the simulation was done for a 5 Ω fault for 10 msec; this resulted in a 176 kJ fault, creating a -270 V deviation (minimum voltage of 11.73 kV, 2.25% below nominal).

http://doi.org/10.24868/issn.2631-8741.2018.008

In each case, the simulated response is lower than what would be predicted through scaling the impulse response; however, the predicted limit on fault energy from the impulse response may be considered as a conservative empirically-derived limit for maintaining compliance.

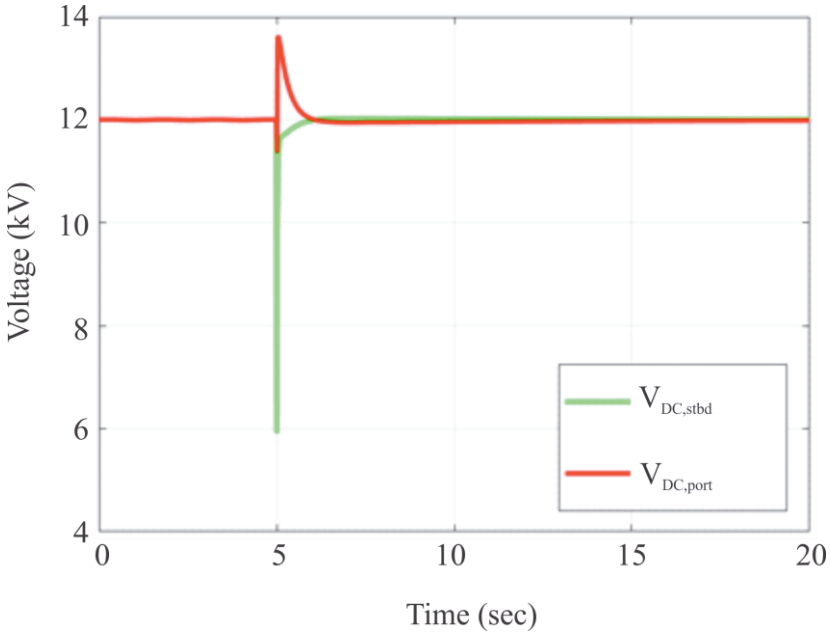

Figure 10: Response in DC bus voltages to a 1Ω fault on the starboard side

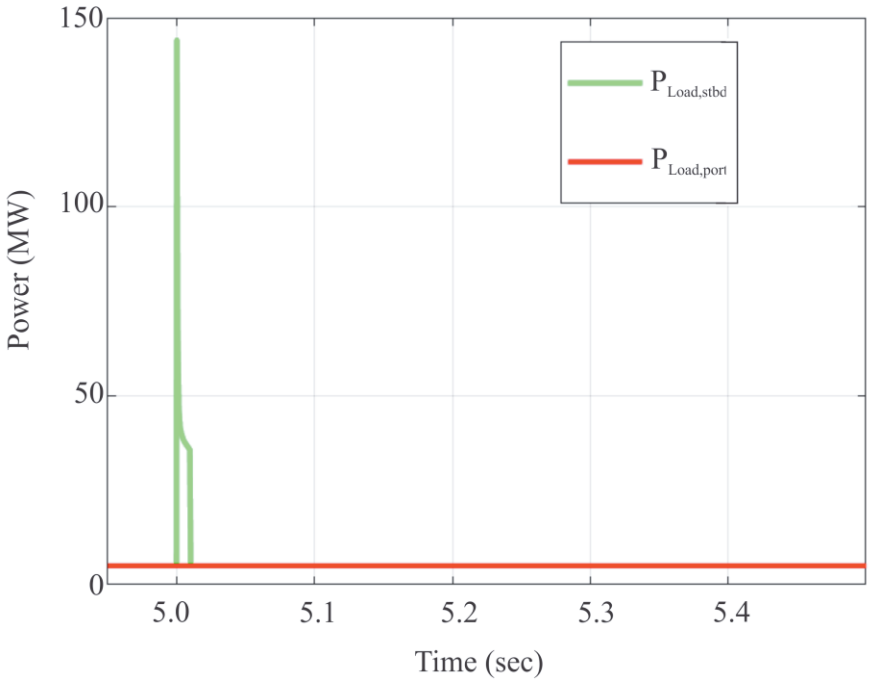

Figure 11: DC bus load power during bus fault simulation showing 1Ω fault on Starboard side

http://doi.org/10.24868/issn.2631-8741.2018.008

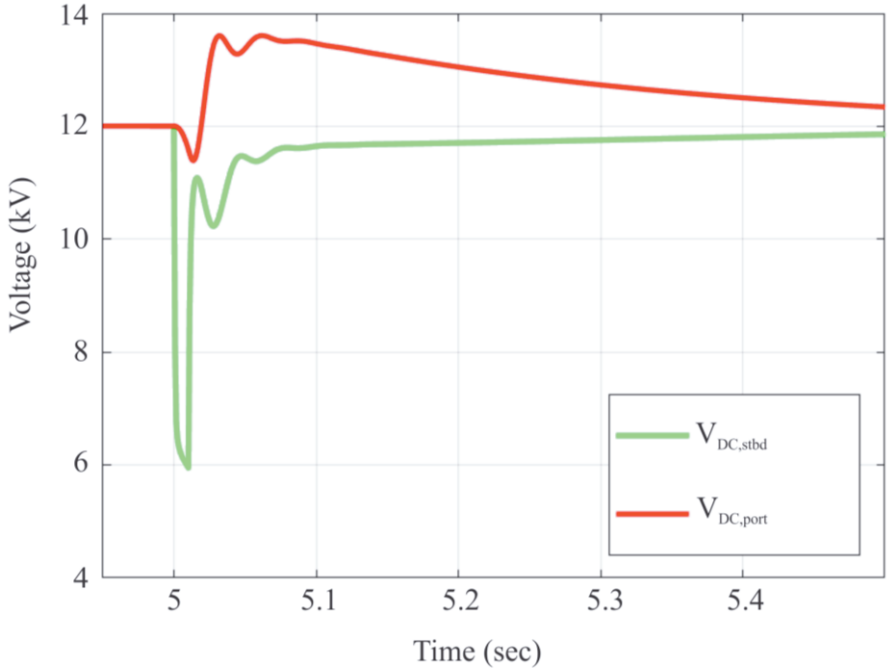

Figure 12: Response in DC bus voltages to a 1Ω fault on the starboard side, focused on the fault response

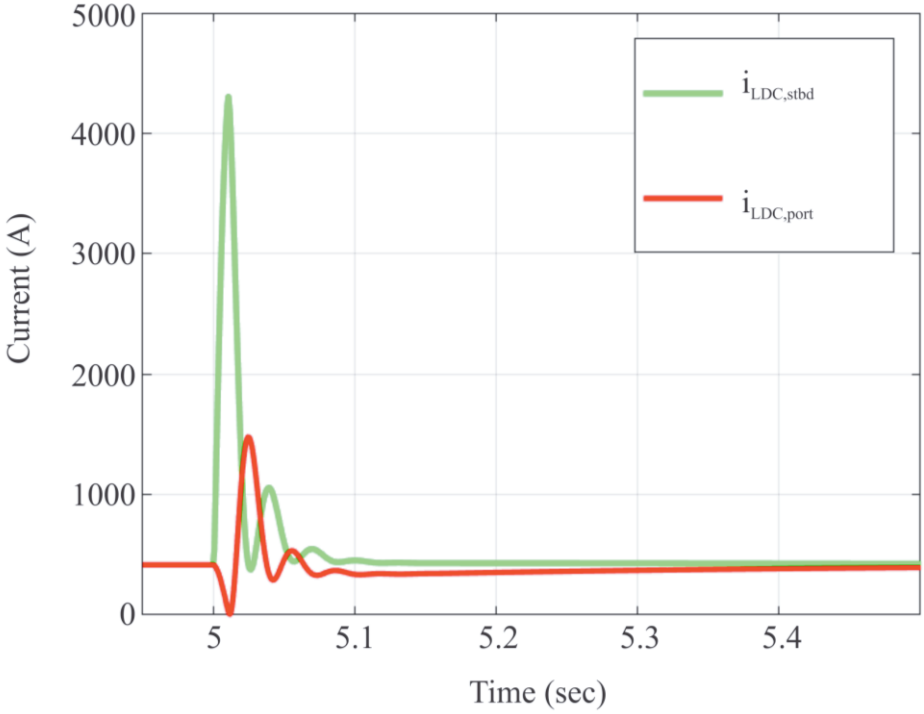

Figure 13: Response in DC bus currents to a 1Ω fault on the starboard side, focused on the fault response

http://doi.org/10.24868/issn.2631-8741.2018.008

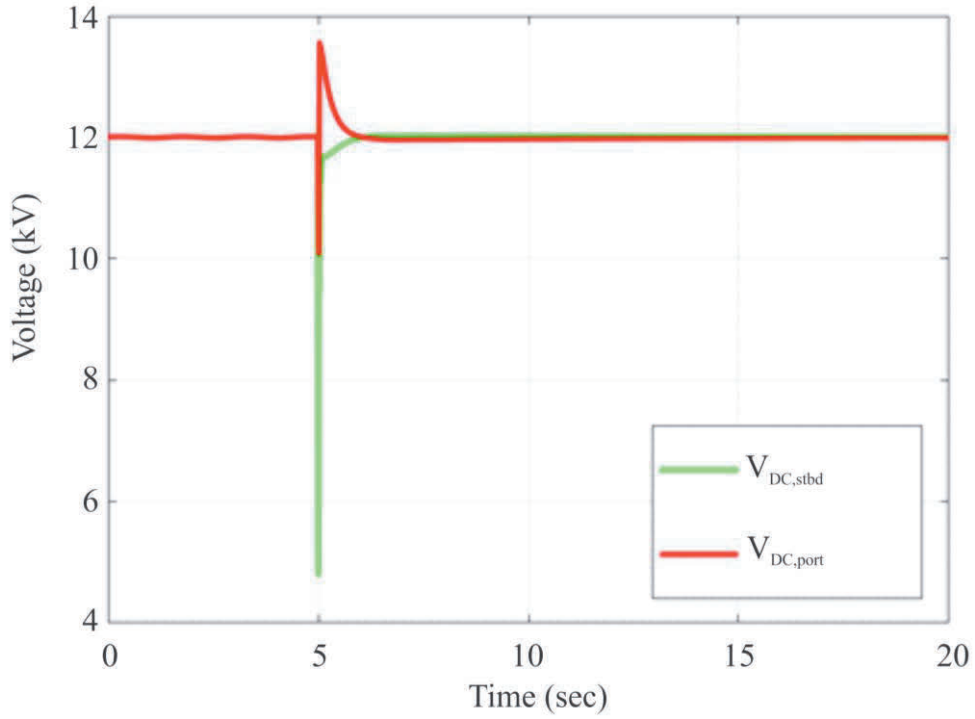

Figure 14: Response in DC bus voltages to a 2Ω fault on the starboard side

6. Conclusions

In this paper, the coupling through a dual wound machine of two DC buses was modelled and simulated, and the results were analysed to draw conclusions on the specifications of the machine and load. In particular, an attempt was made to infer limits on the bus-to-bus coupling and on the stimulus so as to maintain IEEE Std 1709 compliance in the event of a bus fault; specifically, it is desired to maintain the unfaulted bus voltage to within +/- 10% of nominal. As an initial look, a chirp response was done in simulation to identify a coupling transfer function, including a reduced order model. The impulse response of this model was then used to estimate limits on fault energy, and this was compared to simulation results. The simulation results indicated a lower voltage deviation than what was predicted through scaling the impulse response. A difference is to be expected given the different characteristics of large and small signal models. However, the limits predicted by the impulse response could serve as conservative limits to maintain compliance. Specifically, these results are intended to be used to determine the maximum allowable fault current that will not cause the unfaulted bus to violate compliance.

Future work will investigate higher-fidelity (and less conservative) methods of computing limits on fault current. In addition, control methods, such as a current limiting mode in the active rectifier specifications of the generator, will be investigated to further mitigate effects from a faulted bus.

7. Acknowledgements

This work was supported by NAVSEA for a project entitled *Nonlinear Power Flow Control Design for NGIP Energy Storage Requirements*, PR# 1400354102.

The authors also wish to thank Forest White, Todd Hendrickson, Mike Horry, and John Brown for their contributions to the hardware testbed and Dave Wilson for his guidance and leadership on this project.

Sandia National Laboratories is a multi-mission laboratory managed and operated by National Technology and Engineering Solutions of Sandia, LLC., a wholly owned subsidiary of Honeywell International, Inc., for the U.S. Department of Energy's National Nuclear Security Administration under contract DE-NA0003525.

The views expressed in the article do not necessarily represent the views of the U.S. Department of Energy or the United States Government

This paper was approved under SAND number SAND2018-8685 C.

http://doi.org/10.24868/issn.2631-8741.2018.008

8. References

Aghaebramhimi, M. R. and Menzies, R. W. “A Transient Model for the Dual Wound Synchronous Machine,” Canadian Conference on Elect. and Comput. Eng. 1997, vol. 2, pp. 862-865, 1997.

Doerry, N. and Amy, J. Jr., "The Road to MVDC," presented at ASNE Intelligent Ships Symposium 2015, Philadelphia, PA, May 20-21, 2015.

Doktorcik, C. J. “Modeling and Simulation of a Hybrid Ship Power System” M.S. thesis, Dept. Elect. Eng., Purdue Univ., IN, 2011.

Hodge, C. G. and Eastham, J. F. “Dual wound machines for electric ship power systems,” 2015 IEEE Electric Ship Technologies Symposium (ESTS), pp. 62-67, June 2015.

IEEE Recommended Practice for 1 kV to 35 kV Medium-Voltage DC Power Systems on Ships," in *IEEE Std 1709-2010*, pp.1-54, Nov. 2, 2010

Krause, P. C., Wasynczuk, O. and Sudhoff, S. D. Analysis of Electric Machinery and Drive Systems, 2nd ed. Hoboken: John Wiley & Sons, Inc., 2002.

Mese, E. et al., “A permanent magnet synchronous machine with motor and generator functionalities in a single stator core,” Compumag 2013, July 2013.

Mese, E. et al., “Design considerations for dual winding permanent magnet synchronous machines,” 2012 IEEE Energy Conversion Congr. and Expo. (ECCE), pp. 1894-1901, September 2012.

Meyer, R. T., DeCarlo, R. A., Pekarek, S. and Doktorcik, C. J. “Gas Turbine Engine Behavioral Modeling,” School of Elect. Eng., Purdue Univ., West Lafayette, Tech. Rep. TR-ECE-14-01, 2014.

Rashkin, L. J., Neely, J. C., Glover, S. F., McCoy, T. J. and Pekarek, S. D. “Dynamic Considerations of Power System Coupling through Dual-Wound Generators,” 2017 IEEE Electric Ship Technologies Symposium (ESTS), Washington, D.C., 2017, pp. 493-500.

Rashkin, L. J. et al., “Dynamic Response Evaluation of a 20 MW Scale Dual Wound Machine Based Power System,” Advanced Machinery Technology Symposium 2018, Philadelphia, PA, March 28-29, 2018.

 http://doi.org/10.24868/issn.2631-8741.2018.008